Effect of spatially varying material properties on the post-buckling behaviour of composite panels utilising geodesic stochastic fields

SANDER VAN DEN BROEK*, Leibniz University Hannover, Germany
SERGIO MINERA, University of Bristol, United Kingdom
EELCO JANSEN, Leibniz University Hannover, Germany
PAUL M. WEAVER, University of Bristol, United Kingdom and University of Limerick, Ireland
RAIMUND ROLFES, Leibniz University Hannover, Germany

The post-buckling behaviour of panels can be very sensitive to imperfections or variations in materials or geometry. This paper presents an efficient numerical model to calculate the effects of material stiffness variations on the non-linear response of a structure. This is done by first defining a geodesic mesh on which a unit variance random field is generated. This field uses the true geodesic distance on the structure to calculate how points in the field should be correlated. The fields generated are projected onto a 3D structural mesh which is used for assembly and post-processing of the structural model. The structural model, based on the Unified Formulation is capable of accurate non-linear calculations of both straight and curved elements. Baseline results generated using the implementation are compared to those in literature, and verified using Abaqus. Random material variations are then applied to the structure in a Monte Carlo analysis. The analyses show that the local variation of stiffness can have a variety of effects on the non-linear response of structures. Aside from the change of mean stiffness causing a change in bifurcation or limit point load, the different stiffness distributions can affect and trigger competing buckling modes and post-buckling modes and affect their corresponding post-buckling load-deflection paths.

Additional Key Words and Phrases: Imperfections, Variations, Stochastic, Non-Linear, Random Field, Monte Carlo, Composite, Post-Buckling

NOMENCLATURE

Λ	Array with eigenvalues on the diagonal
λ	Eigenvalue
μ	Mean value
ρ	Correlation
σ	Standard deviation
$\boldsymbol{\chi}$	Random vector with unit standard deviation.
θ	Material orientation
cov	covariance operator
$\mathbf{E}$	Correlation matrix
E	Young's modulus
E	Expectation
$\boldsymbol{f}$	Vector with correlated random values
F	Shape function in cross section
$\boldsymbol{g}_i$	Unit vector in axis i
$\mathbf{K}$	Stiffness matrix
$\mathbf{L}$	Decomposed correlation matrix
L_c	Correlation length
m	Exponent used to rescale field
N	Shape function in axial direction
$\mathbf{Q}$	Array with eigenvectors
$\mathbf{R}$	Correlation matrix
$\mathbf{S}$	Second Piola stress tensor
$\boldsymbol{u}$	Displacement field
W_{ext}	External work
W_{int}	Internal energy

*E-mail: s.vandenbroek@isd.uni-hannover.de

1 INTRODUCTION

It has long been the habit of designers to design structures using idealised homogeneous material properties within a structure. The material properties and geometry of real structures are not perfect. Variations in production processes can have an effect on the stiffness of structures due to the curing process (Liu et al. 2006), resulting from variations in fibre orientation (Yurgartis 1987), or from variations in thickness (Sasikumar et al. 2015; Sriramula and Chryssanthopoulos 2013; Kepple et al. 2015). These effects influence the mechanical response of a structure, changing the actual displacement, strains and stresses of real structures according to a distribution which depends on that of the input parameters corresponding to the stiffness and geometrical properties. A considerable number of works on this topic often make use of a distribution of a global input parameter, giving no information of the effect of local variations of this parameter. This in particular holds for variations in material properties. Most research into local variations has focused on variations in geometry (Bielewicz and Górski 2002; Vryzidis, Stefanou, and Papadopoulos 2013; Kriegesmann, Rolfes, Hühne, et al. 2010; Kriegesmann, E. Jansen, and Rolfes 2012; Kriegesmann, Rolfes, E. L. Jansen, et al. 2012; Chen et al. 2016; Schenk and Schuëller 2007). Some researchers have looked into the effects of random variations in material properties, either using shell elements (Papadopoulos and Papadrakakis 2004; Papadopoulos and Papadrakakis 2005), or beam elements (Tootkaboni, Graham-Brady, and Schafer 2009). Higher fidelity models are generally avoided, due to the additional computational cost being prohibitive within Monte Carlo analysis.

The work presented in this paper describes techniques which can be utilised to quantify the variation of the mechanical response. This is done by combining a unified formulation structural model with randomly generated distributions of material parameters. These patterns are generated using a correlation length which is defined using a geodesic length measure within the structure. This allows the correlation of points on a structure to be accurately computed on curved structures. These patterns are mapped back to the structure and used to run Monte Carlo analyses. Running sufficient analyses makes it possible to create a statistical distribution of the response of the non-linear response of a structure. These tools allow designers to analyse how structures might respond to loads when it is manufactured within specified tolerances or manufacturing processes. Using these results can lead to an understanding of the effects of these variations, and gives information to designers on the sensitivity to these variations.

2 METHODS

This section describes the methods used within this paper. This includes a brief description of the structural model, the way random fields are generated and how those are mapped to the structural model.

2.1 Structural approach

The structural model is based on an implementation based on a Unified Formulation, utilising Serendipity Lagrange shape functions (Minera et al. 2018). This model has been extended to include geometric non-linearity and curved elements[1]. This formulation has then been used to do non-linear analyses using Newton-Raphson and arc-length based methods.

2.1.1 Basic formulation. The structural model is a non-linear three-dimensional model. It utilises a displacement field using two different shape functions in the cross-sectional $F(x,z)$ and axial direction $N(y)$.

Starting with a displacement field $\boldsymbol{u} = [u,v,w]^{\mathrm{T}}$ the Green-Lagrange stress tensor $\mathbf{E}$ can be defined as

$$E_{ij} = \frac{1}{2}\left(\boldsymbol{u}_{,i}\cdot\boldsymbol{g}_j + \boldsymbol{u}_{,j}\cdot\boldsymbol{g}_i + \boldsymbol{u}_{,i}\cdot\boldsymbol{u}_{,j}\right) \tag{1}$$

where commas denote derivatives and $\boldsymbol{g}_i$ denotes a unit vector on the i axis. The displacement field $\boldsymbol{u}$ is approximated within the Unified Formulation as

$$\boldsymbol{u}_{(\mathrm{e})}(x,y,z) = F(x,z)N(y)\boldsymbol{u}_i, \qquad \text{with} \qquad i = 1,\ldots,N, \tag{2}$$

where N are the degrees of freedom of the model. For quasi-static problems the elastic equilibrium is

$$\delta W_{\mathrm{int}} = \delta W_{\mathrm{ext}} \tag{3}$$

where W_{ext} and W_{int} are the external work and internal energy. Noting that the internal energy of the structure can be calculated as the sum of internal energy of all the elements $W_{\mathrm{int}} = \sum_e W^{(\mathrm{e})}_{\mathrm{int}}$ the internal energy can be expressed using the stress and strain tensors

$$\delta W^{(\mathrm{e})}_{\mathrm{int}} = \int_{V_{(\mathrm{e})}} \delta\boldsymbol{E}\cdot\mathrm{S}dV \tag{4}$$

where S is the second Piola stress tensor. For non-linear analyses it is of interest to create tangential matrices, the change in internal energy can be written down as (Borst et al. 2012, sec. 3.1.1)

$$\delta(\delta W^{(\mathrm{e})}_{\mathrm{int}}) = \int_{V_{(\mathrm{e})}} \delta\left(\delta\boldsymbol{E}\cdot\boldsymbol{S}\right), dV \tag{5}$$

$$= \int_{V_{(\mathrm{e})}} \delta\boldsymbol{E}\cdot\delta\boldsymbol{S}\, dV + \int_{V_{(\mathrm{e})}} \delta(\delta\boldsymbol{E})\cdot\boldsymbol{S}\, dV \tag{6}$$

where V is the volume of an element. These can be written in terms of a non-linear contribution of the tangential matrix, and geometric stiffness matrix as (Pagani and Carrera 2018)

$$\delta(\delta W^{(\mathrm{e})}_{\mathrm{int}}) = \delta\boldsymbol{u}_j^{\mathrm{T}}\boldsymbol{K}^{(\mathrm{e})}_{(\mathrm{O})ij}\boldsymbol{u}_i + \delta\boldsymbol{u}_j^{\mathrm{T}}\boldsymbol{K}^{(\mathrm{e})}_{(\mathrm{G})ij}\boldsymbol{u}_i. \tag{7}$$

The tangential matrix can then be written as

$$\boldsymbol{K}^{(\mathrm{e})}_{(\mathrm{T})ij} = \boldsymbol{K}^{(\mathrm{e})}_{(\mathrm{O})ij} + \boldsymbol{K}^{(\mathrm{e})}_{(\mathrm{G})ij} \tag{8}$$

where $\boldsymbol{K}^{(\mathrm{e})}_{(\mathrm{O})ij}$ is the non-linear contribution and $\boldsymbol{K}^{(\mathrm{e})}_{(\mathrm{G})ij}$ the geometric stiffness matrix.

[1]The extensions developed by Minera and Patni have been communicated through personal correspondence. The technical details of these extensions will be published in their future works.

2.1.2 Formulation for curved elements. Returning to the displacement field approximation of eq. (2), the model used in the presented research uses Serendipity Lagrange shape functions in the cross section (F), and Lagrange shape functions in the axial (N) direction. These shape functions are used to approximate the displacement field of the structure. The F shape function has either 4, 8, 12, 17, 23 or 30 degrees of freedom per cross section, depending on the order chosen. The current implementation uses four noded beam elements.

Unlike most finite element formulations the choice is made to use different shape functions for the displacement field and the geometry. This allows for a higher fidelity representation of the geometry, without increasing the degrees of freedom of the structural problem. This additional shape function $N^{3D}(\alpha,\beta,\xi)$ is defined within $[-1,1]^3$. These shape functions are usually defined in brick (e.g. 8, 27 or 64 node) elements. The three shape functions N^{3D}, $F(x,z)$ and $N(y)$ are connected through a Jacobian matrix which consists of the shape function's derivatives. These can be interpreted as curvilinear basis vectors.

2.1.3 Non-linear solvers. The problems shown in this paper are solved using either Newton's method or arc length (Riks) method. The implementation is based on (Junuthula Narasimha Reddy 2014, A. 2) and (Lam and Morley 1992). The results presented are generated using updated tangential matrices at each iteration.

The arc-length approach uses a circular constraint, and converges using Newton's method between each converged step.

2.2 Assigning random material variations

The variations analysed in this paper are generated and applied by combining a number of different techniques and methods. The choice has been made to generate random fields correlated to the geodesic distance of the structure. This approach does make the generation and mapping more complex. This section will discuss the methods used to generate the geodesic distance array, generate the field and how it is mapped to the structure.

2.2.1 Geodesics. The geodesic length refers to the length as it would be on a surface. This differs from the Euclidean length, which calculates the distance between two coordinates in space as a straight line. The easiest approach for this problem would be to find the shortest path between two points using the connectivity of a mesh. This can be done by searching for the point by slowly moving away from the origin point in all directions until the other point has been found. This approach was published by Dijkstra 1959, but has a tendency to overestimate the distance. This is because the shortest distance usually crosses over the face of an element (usually a polyhedron). Finding the actual shortest distance over a mesh is a classic field of research in computational geometry, with many approaches being proposed and extended on over the years (Bose et al. 2011). The approach used within this paper is based on the idea first published by Varadhan 1967 and recently extended by Crane, Weischedel, and Wardetzky 2017. In this approach heat is introduced at a point on a mesh for a time t, this generates a vector field of the heat flux on the surface. This vector field is normalised, after which the distance is calculated by solving the Poisson heat equation. Crane has shown how this approach can be prefactored, greatly reducing the computational time when distances between many points are required, as is the case for random fields.

Within the current implementation a shell mesh is generated within the structure. This is done using coordinates in the cross section, which are then projected using mapping functions. Alternatively a mesh can be generated manually within a mesher and used to generate the random field.

2.2.2 Generating random fields. Random fields are stochastically generated distributions of a parameter in n dimensional space. The fields generated within this work are generated on a 2D plane within 3D space. The values of these random variables are not completely unrelated to each other, actual variations are usually related to the variations around it. This is why the geodesic length of section 2.2.1 is used as a parameter to relate points. There are many different techniques to generate random fields (Spanos and Zeldin 1998). Many of these methods have assumptions in the space or correlation function. The method that is used within this work is called Covariance Matrix Decomposition (CMD), and has the advantage of its relative ease in which other correlation functions can be used, and with which geodesic length can be included.

The correlation of two sets X and Y is defined mathematically as (Dekking et al. 2005, ch. 10)

$$\rho_{X,Y} = \frac{\mathrm{cov}(X,Y)}{\sigma_X \sigma_Y} = \frac{\mathrm{E}[(X-\mu_X)(Y-\mu_Y)]}{\sigma_X \sigma_Y}. \tag{9}$$

where ρ is the correlation, cov the covariance operator and E the expectation operator.Within random fields these sets could be seen as two points of the field, and how they are related with a sufficiently large sample size. The correlation varies between 1 and -1, and indicates the relationship between two sets. For generating random fields it is useful to define functions, which define the correlation as a function of distance. The fields generated in this paper are generated using the correlation function

$$\rho_{s,exp} = e^{-\left(\frac{\Delta L}{L_c}\right)^2}, \tag{10}$$

in which L_c is called the correlation length, and ΔL the (geodesic) distance between two points.

The CMD method uses discretised points in space and assigns a random value to that value (Davis 1987). It is important that the field is discretised fine enough to represent the transition in variation amplitude. The necessary refinement was studied by Li and Der Kiureghian 1993 and found to be between $\frac{L_c}{4}$ and $\frac{L_c}{2}$ for the correlation function of eq. (10).

The CMD method decomposes the correlation matrix. This decomposed matrix can be used to calculate random fields through simple multiplication with a random vector $\boldsymbol{\chi}$ with unit variance and zero mean. The first step in generating fields is to build a correlation matrix of all points y_i of the field,

$$R_{ij} = \frac{\mathrm{cov}(y_i,y_j)}{\sqrt{\sigma_{y_i}\sigma_{y_j}}} \rightarrow \mathbf{R} = \begin{bmatrix} 1 & \rho(y_1,y_2) & \dots & \rho(y_1,y_n) \\ \rho(y_2,y_1) & 1 & \dots & \rho(y_2,y_n) \\ \vdots & & \ddots & \vdots \\ \rho(y_n,y_1) & \rho(y_2,y_n) & \dots & \rho(y_n,y_n) \end{bmatrix} \tag{11}$$

where $\rho(y_i,y_j) = \rho(y_j,y_i)$, noting that the correlation here can be calculated using eq. (10).

Taking the definition of covariance

$$\mathrm{cov}\left[X,Y\right] = \mathrm{E}\left[XY\right] - \mathrm{E}\left[X\right]\mathrm{E}\left[Y\right] \tag{12}$$

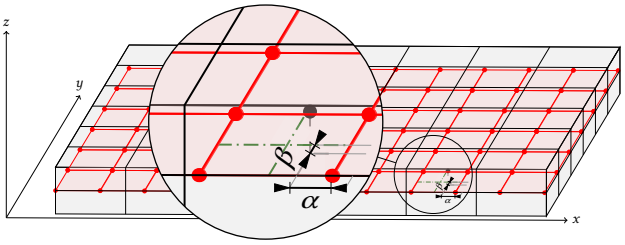

Fig. 1. Mapping between random field and geometrical brick elements

and keeping in mind the field has mean of zero, it is possible to show that $\mathbf{R}$ can be decomposed into two matrices.

$$\begin{aligned} \mathbf{R} &= \mathrm{cov}[\boldsymbol{x},\boldsymbol{x}] = \mathrm{E}(\boldsymbol{x},\boldsymbol{x}^T) - 0 \cdot 0 \\ &= \mathrm{E}(\mathbf{L}\boldsymbol{\chi}\mathbf{L}\boldsymbol{\chi}^T) = \mathbf{L}\mathrm{E}(\boldsymbol{\chi}\boldsymbol{\chi}^T)\mathbf{L}^T = \mathbf{L}\mathbf{I}\mathbf{L}^T = \mathbf{L}\mathbf{L}^T \end{aligned} \tag{13}$$

From eqs. (10) and (11) the matrix $\mathbf{R}$ is symmetric and positive definite, the eigenvalues should all be positive and real. This decomposition is done by using eigendecomposition in the form of

$$\mathbf{R} = \mathbf{Q}\boldsymbol{\Lambda}\mathbf{Q} \tag{14}$$

in which $\boldsymbol{\Lambda}$ is a diagonal matrix with the eigenvalues of $\mathbf{R}$, and $\mathbf{Q}$ contains the eigenvectors of the matrix. The matrix $\mathbf{L}$ can be extracted from this:

$$\mathbf{R} = \mathbf{Q}\hat{\boldsymbol{\Lambda}}\hat{\boldsymbol{\Lambda}}\mathbf{Q} = \mathbf{L}\mathbf{L}^T \rightarrow \mathbf{L} = \mathbf{Q}\hat{\boldsymbol{\Lambda}} \tag{15}$$

in which $\hat{\boldsymbol{\Lambda}} = \mathrm{diag}(\sqrt{\lambda})$, in which λ are the eigenvalues of the $\mathbf{R}$ matrix. Using the decomposed correlation matrix $\mathbf{L}$ it is possible to generate random fields using

$$\mathbf{f} = \mathbf{L}\boldsymbol{\chi}. \tag{16}$$

This makes it possible to generate a large amount of fields, with the main computational costs being in pre-factoring.

2.2.3 Mapping random fields to structure. Using the methods described in the previous sections, 2D (surface) fields are generated within a 3D space. The structural model has an additional dimension (thickness). The assumption is made that the variation through thickness is negligible, and constant properties are used for every material through thickness[2]. The choice was made to use the 3D brick elements described in section 2.1.2 to evaluate the field within the geometry of an element. This approach allows the field and the structure to be discretised independently. Certain structures with a lot of curvature may benefit from a finely discretised random field (as the geodesic length would be more accurate) while not needing a large refinement in structural elements to converge to accurate results.

During initialisation of the analysis the nodes of the brick element are projected to the nearest location on the field. During this, the random field element number and local coordinates associated with every brick node are stored. This makes it possible to quickly compute the values associated with those nodes when an analysis is started, using quadrilateral shape functions for the random field mesh. This process is illustrated in fig. 1, where eight node brick elements are used. It is still necessary to have shape functions in the brick elements that can describe the field values accurately. Using higher order brick functions (e.g. 27 nodes) makes it possible to reproduce more complex distributions throughout the volume. During assembly, the material properties are assigned as

[2]It is still possible to have different materials through thickness.

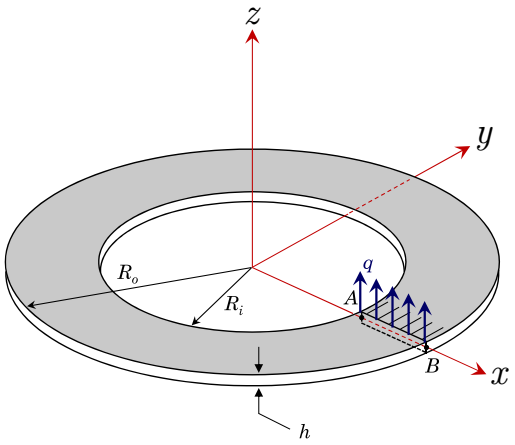

Fig. 2. Annular slit under vertical shear force, adapted from Payette and J. N. Reddy 2014, fig. 14

$$E_{pt} = E_\mu + x_{pt} E_\sigma \tag{17}$$

in which E_{pt} is the Young's modulus at point $_{pt}$, E_μ is the mean value of E, x_{pt} is the value of the random field at the point and E_σ is the standard deviation of the parameter E. The same holds true for any other material parameter (such as fibre angle).

3 ANALYSES

The methods described in the previous section were used on a number of different examples. The first examples show the effect of variations on force-displacement of an annular slit ring under shear. The second problem analysed is a flat plate under compression, in which membrane effects are more dominant. The final examples are of a curved panel.

3.1 Annular ring under shear (isotropic)

3.1.1 Description. This example has been taken from Payette and J. N. Reddy 2014, sec. 6.3. It consists of an annular ring with a slit. One of the edges is clamped, the other is subjected to a shear force. The structure is illustrated in fig. 2. The dimensions are $h = 0.03$ m, $R_i = 6$ m $R_0 = 10$ m. The structure is discretised into 10 elements along the cross section, and 20 elements in axial direction. The system has a total of 15 372 degrees of freedom, and takes an average of 22 minutes to solve using a single computational thread. Using 32 computational cores on the Blue Crystal phase 3 cluster it takes an average of 41 seconds per run. The material properties used are $E_\mu = 21 \cdot 10^6$ and $\nu = 0$. The Young's modulus is varied with a standard deviation of $E_\sigma = 420$ kPa, equating to a coefficient of variation of 2%. The fields are generated using a correlation length $L_c = 1$ m.

This structure does not buckle, but serves as a reference to verify the non-linear solver and analyse the behaviour of material variations on the displacement results within a geometrically non-linear setting. Using the geodesic length means that the actual length on the ring is used for calculating the correlation, not the Euclidian length.

3.1.2 Numerical results. The analysis is repeated 2000 times and solved using a Newton scheme and third order shape functions. The unscaled final deformation of the structure is shown in fig. 3, showing the highly non-linear deformation of the structure. An example of the material distribution is found in fig. 4. Figure 5

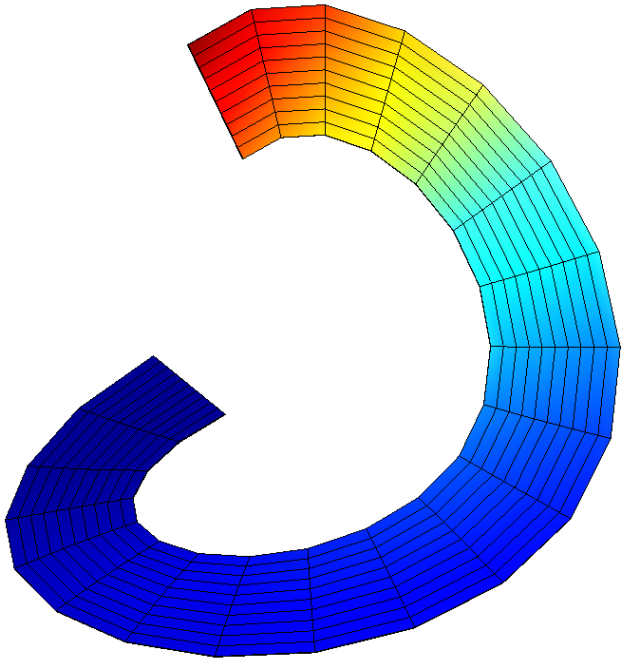

Fig. 3. Deformed isotropic annular ring at a shear load of 26 Pa

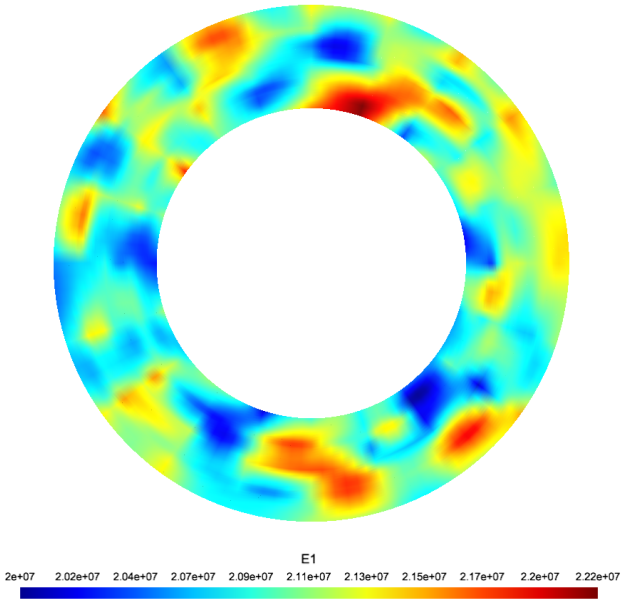

Fig. 4. Young's modulus distribution within one sample run

has the force-displacement graph of the baseline (homogeneous) results and those found in (Payette and J. N. Reddy 2014, sec. 6.3), showing good agreement. An analysis of the variation in the force-displacement graph shows that the overall displacement of the structure at point A does not vary a lot during the Monte Carlo analysis using random sampling. All runs are shown within one figure in fig. 6.

An analysis of the components of the total displacement reveals that there is one component in which the displacement result has a higher relative spread, the y-component shown in fig. 7. This can be explained by x-displacement being susceptible to

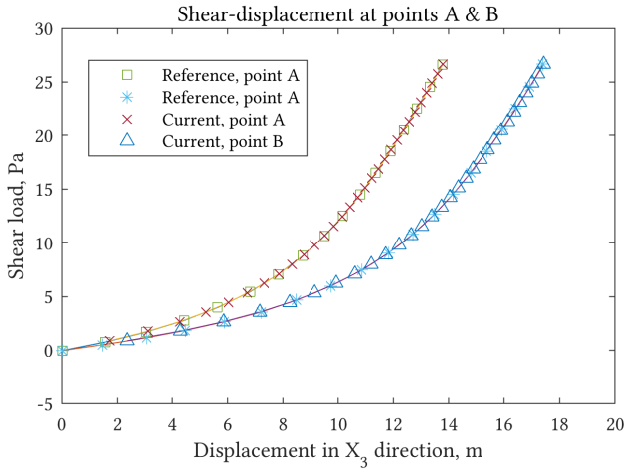

Fig. 5. Comparison of shear-displacement of unified model and results of Payette and J. N. Reddy 2014 at points A and B of fig. 2

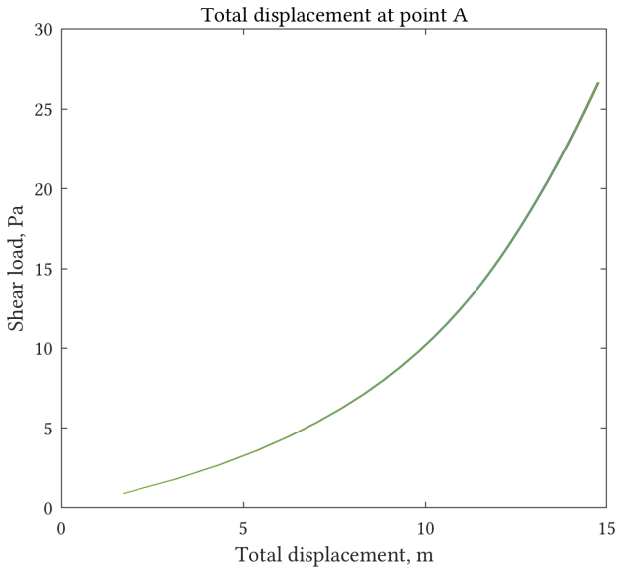

Fig. 6. Monte Carlo results of total displacements at point A of fig. 2

local variations close to the boundary condition. The y position of the end point is largely dependent on how the structure curves close to the boundary condition. This makes it sensitive to local variations in that area. Analysing the other components, the z-displacement is dominated by the stiffness of the total structure (as this is the load direction). The x-displacement is dominated by the the geometric non-linear response, it is not highly loaded causing the stiffness variation to have only a small contribution to the response.

3.2 Annular ring under shear (composite)

3.2.1 Description. This problem uses the same geometry as section 3.1, but uses the material properties found in table 1. The structure is split into three equal layers with a 90-0-90 degree orientation. This is modelled using 10x3 third order elements in the cross section and 20 elements in the axial direction. The system has a total of 34 770 degrees of freedom. Using 32 computational

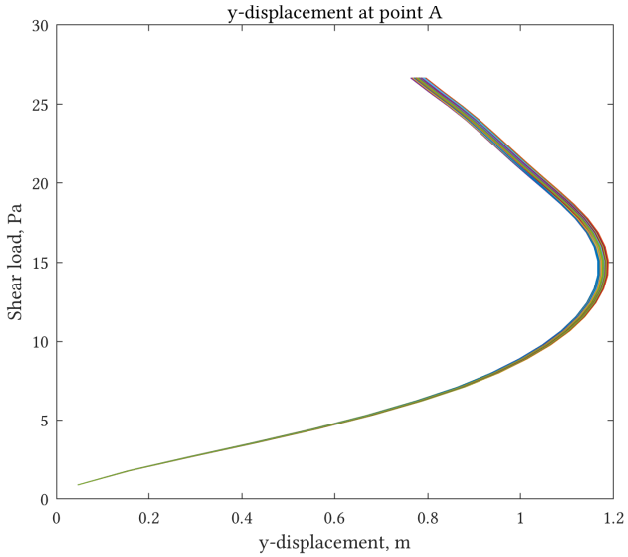

Fig. 7. Y-displacement results of point A

Material properties			
E_1	20 MPa	$E_2 = E_3$	6 MPa
G_{23}	2.4 MPa	$G_{13} = G_{12}$	3 MPa
ν_{23}	0.25	$\nu_{23} = \nu_{12}$	0.3

Table 1. Material properties for composite examples, taken from Payette and J. N. Reddy 2014

cores on the Blue Crystal phase 3 cluster it takes an average of 86.4 seconds per run.

Instead of varying the Young's modulus the fibre orientation is varied. This is done with a standard deviation of $\theta_\sigma = 2°$. This is the upper range of the measurements found by Yurgartis 1987. These variations are applied to each layer separately, with a correlation length of $L_c = 1$ m.

3.2.2 Numerical results. As was the case for the isotropic results, the composite results were first compared to those found in (Payette and J. N. Reddy 2014), this comparison can be found in fig. 8, and shows good agreement. A Newton solver was used to solve all 2000 runs of the structure using load control. The general trend shown in fig. 9 in the displacement fields are the same as the isotropic case, but the displacements diverge more as the load increases. This effect is particularly visible in the y-displacements shown in fig. 10. This can be explained by the misalignments causing bend-twist coupling, which affect the displacement field.

3.3 Flat panel (isotropic)

3.3.1 Description. This analysis is on the 600x200x1 mm flat panel shown in fig. 11. Out of plane displacements are restricted on all the edges and rigid body modes are restricted through two point constraints. The model is discretised into a 16x1 element cross section and 24 elements in the axial direction. The system has a total of 28 908 degrees of freedom. Using 32 computational cores on the Blue Crystal phase 3 cluster it takes an average of 66.7 seconds per run.

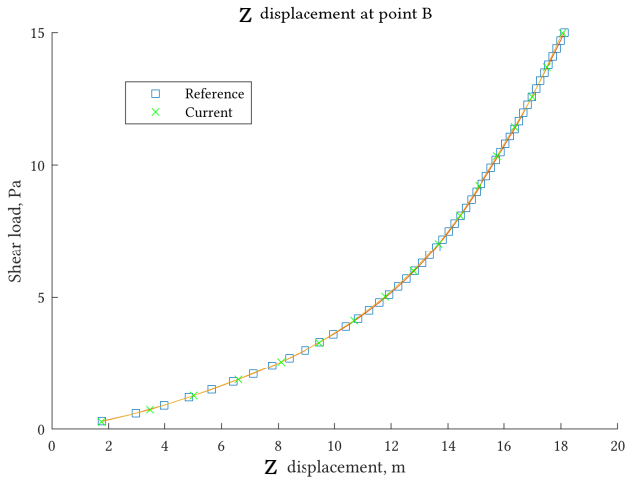

Fig. 8. Results of current implementation compared to that of (Payette and J. N. Reddy 2014) showing z-displacement at point B in fig. 2.

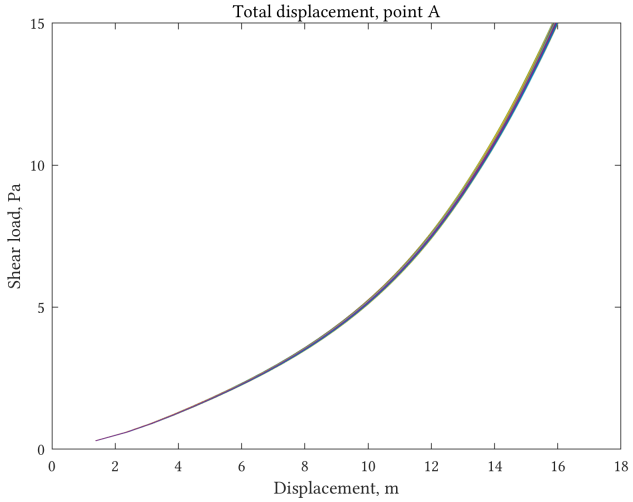

Fig. 9. Total displacement of composite ring of point A in fig. 2

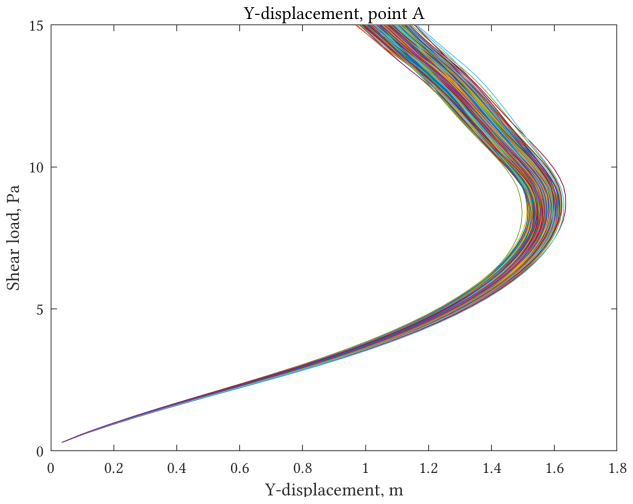

Fig. 10. Y-displacement response of composite ring at point A in fig. 2

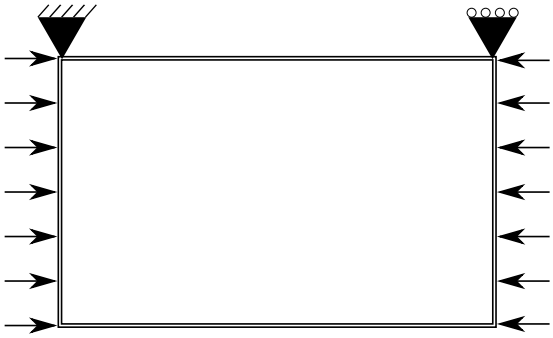

Fig. 11. Free body diagram of flat plate

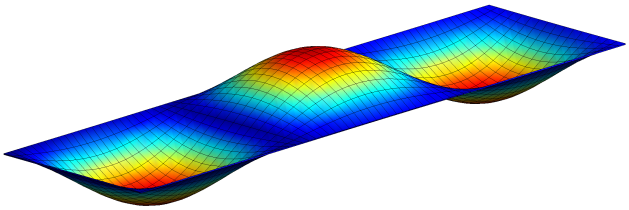

Fig. 12. First linear buckling mode of flat panel structure

The material properties used are $E_\mu = 181$ GPa and $\nu = 0.3$. A geometric imperfection is applied in the shape of the first buckling mode (fig. 12) of the baseline result, with an amplitude of 5% of the thickness. The baseline linear buckling load is 3.23 kN and was verified using Abaqus. Variations in the Young's modulus are applied with a standard deviation of $E_\sigma = 1.81$ GPa (CoV 1%). The correlation length of these imperfections is 100 mm.

3.3.2 Numerical results. The analysis was performed 2000 times and solved using Newton's approach utilising increments in the load level. The out of plane displacement in the centre of the plate (100,200,0) mm is shown in fig. 13. The results show less shifting in the buckling mode than was found in previous work (Broek et al. 2017). This is most likely due to the 5% geometric imperfection dominating the post-buckling shape.

3.4 Curved panel (isotropic)

The structures analysed thus far consist of flat geometry. This analysis instead focuses on a curved panel. The panel has a radius of 100 mm, is 2 mm thick and 150 mm in length. The geometry is illustrated in fig. 14. It is discretised in 10x1 third order elements in the cross section and 10 elements in the axial direction. There are 7 812 degrees of freedom. The problem is solved using an arc-length approach, taking 30 minutes using a single computational thread. Using 32 threads on the Blue Crystal phase 3 cluster, a run is completed every 56 seconds. The structure is constrained in out of plane displacement on the edges on which load is introduced. Axial displacement is constrained by constraining two points on one of the loaded edges in the axial (y) direction. The usage of geodesic length in the generation of random fields means that the curvature of the structure is taken into account in the generation of the field.

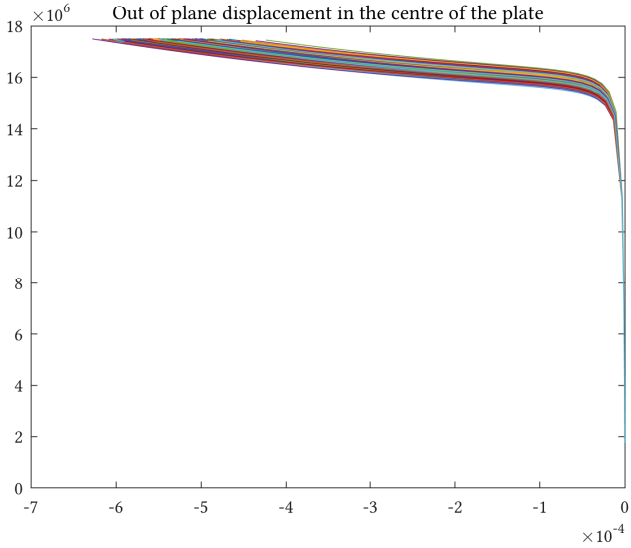

Fig. 13. Out of plane displacement in centre of the plate

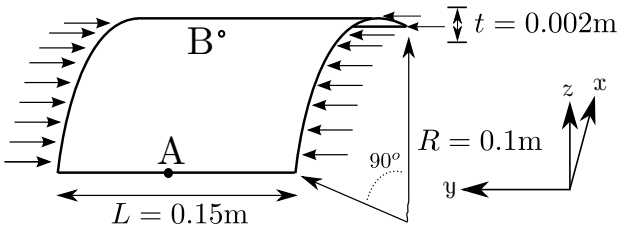

Fig. 14. Geometry of the curved panel

3.4.1 Description. The material properties are the same as the flat panel of section 3.3, with $E_\mu = 181$ GPa and $\nu = 0.3$. The linear buckling load of 569.6 MPa (178 930 N) was verified in Abaqus.

The Young's modulus is varied with $E_\sigma = 1.81$ GPa, equivalent to a 1% coefficient of variation. The correlation length used to generate the fields is $L_c = 0.025$ m. Non-linear analyses are run 2000 times using an arc-length based solution algorithm.

3.4.2 Numerical results. The behaviour of the structure in post-buckling is characterised by two dominant shapes found in fig. 15. The pre-buckling displacement is symmetric on the y-z plane, as shown in fig. 15a The non-homogeneous stiffness distribution causes one side of the panel to dominate in post-buckling. This leads to an asymmetric post-buckling shape in which one of the edges becomes dominant, as shown in fig. 15b. This tendency to deviate from the symmetric solution is best illustrated by fig. 16, where the asymmetric stiffness in the structure clearly shifts the centre of the structure to one side, instigating the out of plane behaviour on that side.

The z-displacement at the middle of the straight edge (A in fig. 14) is shown in fig. 17. This force-displacement graph shows the three main possibilities for the load-displacement path of point A in the structure. Which of the three possibilities will occur, depends on the stiffness distribution of the structure. In the neighbourhood of the critical load level, the stiffness of the structure strongly changes and the structure buckles at a limit point. Subsequently, depending on the buckling deformation, point A follows one of three main paths:

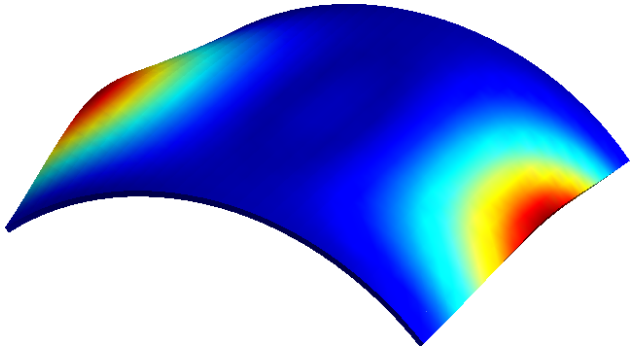

(a) Symmetric mode, taken from the baseline (homogeneous) run in post-buckling

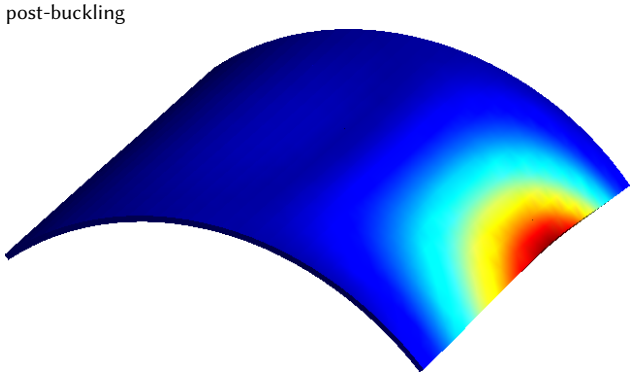

(b) Asymmetric mode, Post-buckling from a run with material variations

Fig. 15. Dominant displacement fields found in the non-linear response

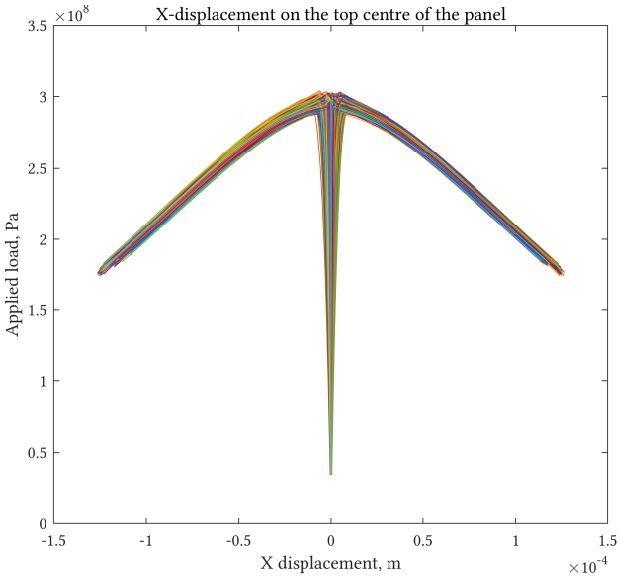

Fig. 16. X-displacement in the centre of the panel, point B in fig. 14

Asymmetric stiffness If the side of the panel with point A corresponds to a strong buckling deformation (the "weak side"), this side will dominate in out of plane displacement. Alternatively, point A is on the "stiff side" of the structure. The deflection on this side of the panel will reverse and reduce.

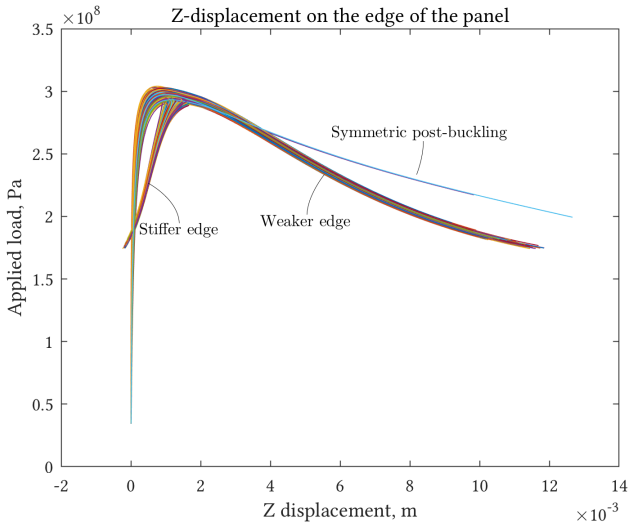

Fig. 17. Z-displacement in the edge of the panel, point A in fig. 14

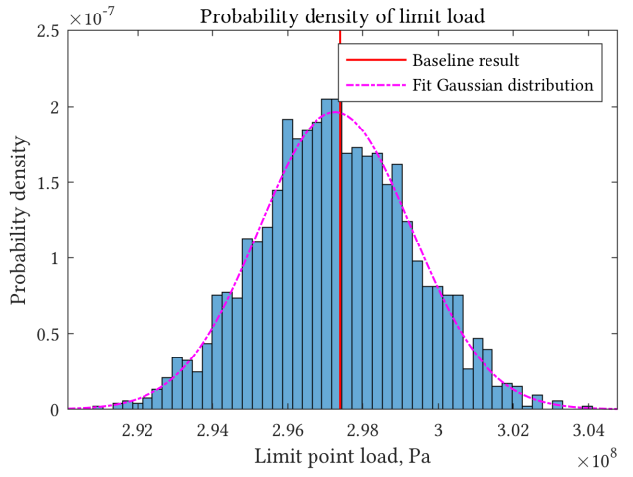

Fig. 18. Probability density function of limit point load of the isotropic curved panel

Symmetric stiffness In the rare case that the stiffness distribution of the structure remains nearly symmetric (only 0.1% of runs), a symmetric deflection of the structure will continue to dominate. This corresponds to a less steep decline in the load-displacement curve.

In all three cases the post-buckling behaviour is unstable.

Another thing that is of interest is the limit point load of the structure, particularly since the post-buckling behaviour is unstable. A probability density plot of the limit point load is shown in fig. 18. The mean and standard deviation of the limit load are $F_\mu = 297.3$ MPa and $F_\sigma = 2$ MPa, which equates to a coefficient of variation of 0.7%. This is less than the coefficient of variation of the input parameter, which indicates that local variations of the Young's modulus do not dominate the distribution of the limit point load.

3.5 Curved panel (composite)

The final analysis discussed in this paper analyses the same structure as the previous example, but uses a simple composite layup.

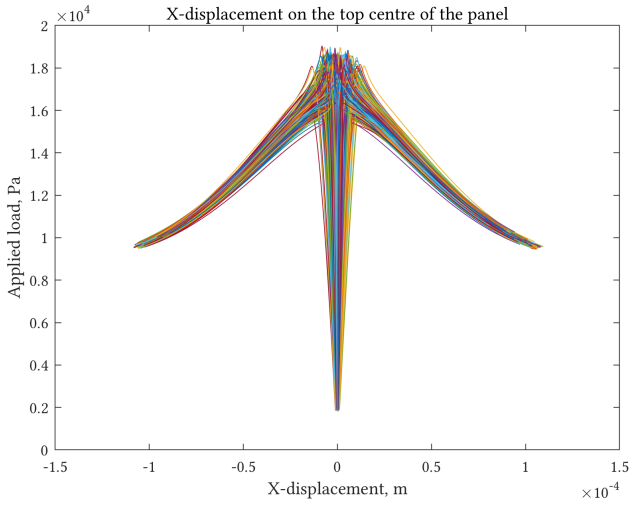

Fig. 19. X-displacement at point A of the composite curved panel

The variations are applied to the fibre angle θ instead of the Young's modulus.

3.5.1 Description. As previously mentioned this example uses geometry identical to that used in section 3.4. Instead of isotropic material properties the properties of table 1 are used. The structure is split into three equal layers with a 90-0-90 degree orientation. The cross section is discretised using 10x3 third order elements, and 10 elements in the axial direction. The structure has a total of 17 670 degrees of freedom. The structure is solved using an arc-length solver, taking an average of 205 seconds per run using 32 computational threads on the Blue Crystal Phase 3 computing cluster.

The fibre orientation is varied instead of the Young's modulus. This is done with a standard deviation of $\theta_\sigma = 2°$. This is the upper range of the measurements found by Yurgartis 1987. These variations are applied to each layer separately, with a correlation length of $L_c = 0.025$ m.

3.5.2 Numerical results. The analysis was run 1600 times, the trends seen are similar to those found in section 3.2. The x-displacement at point A (centre) shows the two post-buckling paths, fig. 19. The paths are similar to those of the isotropic case.

Looking at the z-displacement of the edge in fig. 20 the three branches described in section 3.4 can be seen once more. The symmetric load path diverges from the asymmetric branch later in later in the graph, there is also more curvature in the non-dominant path. Both of these responses are most likely due to the asymmetric bending stiffness of the laminate. The 90-0-90 layup causes the bending stiffness in the axial direction to be less stiff. It is likely that these affect post-buckling behaviour either delay or stimulate the creation of such features depending on whether or not energy can be stored within the structure during the load application.

Figure 21 shows the distribution of the limit point load of the composite panel. The spread is much more significant than the isotropic case under a 2% variation in Young's modulus (fig. 18). The mean buckling load of $F_\mu = 17\,438$ Pa is 0.6% less than that found in the baseline result of $F_{\text{BL}} = 17\,540$. The standard deviation of the limit point load $F_\sigma = 566$ Pa, which equates to a coefficient of variation of 3.25%. This is significantly more than

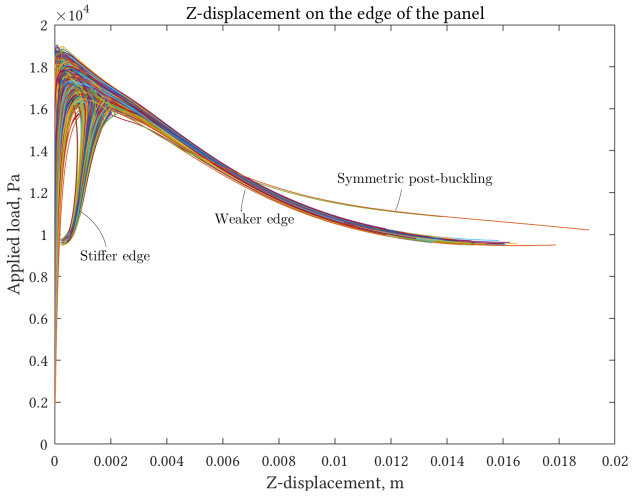

Fig. 20. X-displacement at point B of the composite curved panel

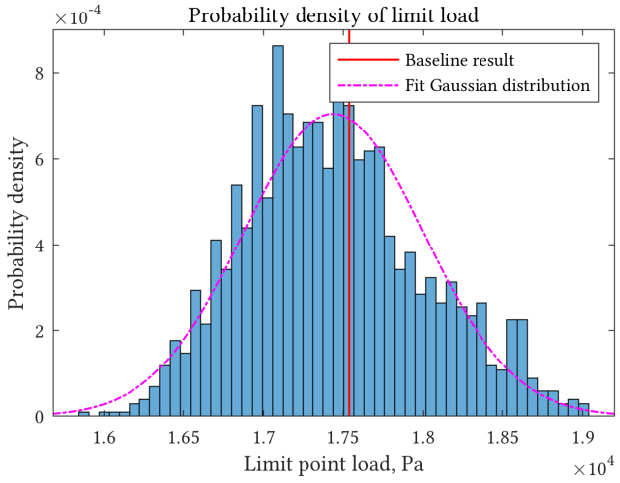

Fig. 21. Probability density function of limit point load of the composite curved panel

that of the isotropic example, especially when considering that the three layers of the structure have independently generated fields. This indicates that the fibre orientation has a larger effect than the Young's modulus of the isotropic structure.

4 CONCLUSIONS

This contribution presented examples on how material property variations can affect the non-linear response of panel-type structures, including structures with curvature. The stochastic analysis of these responses was done in an approach which includes the use of a geodesic length measure, which makes the approach usable for a wide range of (highly) curved structures. The versatility and capabilities of the approach was demonstrated by its application on a variety of structures and materials.

The examples presented show that local variations in stiffness of a structure can have a variety of effects on its non-linear response. Aside from the change of mean stiffness causing a change in bifurcation or limit point load, it was also shown that the different stiffness distributions can affect and trigger competing buckling modes and post-buckling modes and their corresponding post-buckling load-deflection paths.

The tools developed could be used in future research to analyse the sensitivity of structures to variations and in such a way tailor the structure to specific post-buckling paths, decrease sensitivity to variations or increase the limit point load. Combining the analysis approach with design and manufacturing tools makes it possible to achieve realistic variations of the stiffness within a structure in order to make structures more robust and better performing, similar to approaches proposed by Cox et al. 2018 for tailoring post-buckling of structures using modal nudging or Haldar et al. 2018 to tailor snap-through loads of Variable Stiffness laminates.

ACKNOWLEDGEMENTS

This project has received funding from the European Union's Horizon 2020 research and innovation program under the Marie Skłodowska-Curie grant agreement No. 642121.

This work was carried out using the computational facilities of the Advanced Computing Research Centre, University of Bristol - http://www.bris.ac.uk/acrc/ as well as computational facilities within the Institute of Structural Analysis at Leibniz University Hannover.

REFERENCES

Bielewicz, Eugeniusz and Jarosław Górski (2002). "Shells with random geometric imperfections simulation - Based approach". In: *International Journal of Non-Linear Mechanics* 37.4-5, pp. 777–784. ISSN: 00207462. DOI: 10.1016/S0020-7462(01)00098-1.

Borst, René de, Mike A. Crisfield, Joris J. C. Remmers, and Clemens V. Verhoosel (2012). *Non-Linear Finite Element Analysis of Solids and Structures*. Sussex, United Kingdom: Wiley. ISBN: 9781118375938. DOI: 10.1002/9781118375938. URL: http://doi.wiley.com/10.1002/9781118375938.

Bose, Prosenjit, Anil Maheshwari, Chang Shu, and Stefanie Wuhrer (2011). "A survey of geodesic paths on 3D surfaces". In: *Computational Geometry: Theory and Applications* 44.9, pp. 486–498. ISSN: 09257721. DOI: 10.1016/j.comgeo.2011.05.006. URL: http://dx.doi.org/10.1016/j.comgeo.2011.05.006.

Broek, Sander van den, Eelco Jansen, Tanvir Rahman, and Raimund Rolfes (2017). "Effect of spatially varying stochastic material properties on the post- buckling behavior of composite panels using a reduced order model". In: *ECCOMAS Thematic Conference on the Mechanical Response of Composites*.

Chen, Gengbo, Hao Zhang, Kim J.R. Rasmussen, and Feng Fan (2016). "Modeling geometric imperfections for reticulated shell structures using random field theory". In: *Engineering Structures* 126, pp. 481–489. ISSN: 01410296. DOI: 10.1016/j.engstruct.2016.08.008. URL: http://linkinghub.elsevier.com/retrieve/pii/S0141029616304102.

Cox, B. S., R. M.J. Groh, D. Avitabile, and A. Pirrera (2018). "Modal nudging in nonlinear elasticity: Tailoring the elastic post-buckling behaviour of engineering structures". In: *Journal of the Mechanics and Physics of Solids* 116, pp. 135–149. ISSN: 00225096. DOI: 10.1016/j.jmps.2018.03.025. URL: https://doi.org/10.1016/j.jmps.2018.03.025.

Crane, Keenan, Clarisse Weischedel, and Max Wardetzky (2017). "The Heat Method for Distance Computation". In: *Communications of the ACM* 60.11, pp. 90–99. ISSN: 0001-0782 (print), 1557-7317 (electronic). DOI: https://doi.org/10.1145/3131280.

Davis, Michael W. (1987). "Production of conditional simulations via the LU triangular decomposition of the covariance matrix". In: *Mathematical Geology* 19.2, pp. 91–98. ISSN: 08828121. DOI: 10.1007/BF00898189.

Dekking, Frederik Michel, Cornelis Kraaikamp, Hendrik Paul Lopuhaä, and Ludolf Erwin Meester (2005). *A Modern Introduction to Probability and Statistics: Understanding why and how*. Springer Science & Business Media. ISBN: 9781846281686.

Dijkstra, E. W. (1959). "A note on two problems in connexion with graphs". In: *Numerische Mathematik* 1.1, pp. 269–271. ISSN: 0029599X. DOI: 10.1007/BF01386390.

Haldar, Ayan, Eelco Jansen, Raimund Rolfes, and Paul Weaver (2018). "Tailoring Snap-through Loads in Variable Stiffness Composites". In: *2018 AIAA/ASCE/AHS/ASC Structures, Structural Dynamics, and Materials Conference*. AIAA SciTech Forum. American Institute of Aeronautics and Astronautics. DOI: doi: 10.2514/6.2018-2245. URL: https://doi.org/10.2514/6.2018-2245.

Kepple, Jendi, Manudha T Herath, Garth Pearce, B. Gangadhara Prusty, Rodney Thomson, and Richard Degenhardt (2015). "Stochastic analysis of imperfection sensitive unstiffened composite cylinders using realistic imperfection models". In: *Composite Structures* 126, pp. 159–173. ISSN: 02638223. DOI: 10.1016/j.compstruct.2015.02.063. URL: http://dx.doi.org/10.1016/j.compstruct.2015.02.063.

Kriegesmann, Benedikt, Eelco Jansen, and Raimund Rolfes (2012). "Semi-analytic probabilistic analysis of axially compressed stiffened composite panels". In: *Composite Structures* 94.2, pp. 654–663. ISSN: 02638223. DOI: 10.1016/j.compstruct.2011.08.033. URL: http://dx.doi.org/10.1016/j.compstruct.2011.08.033.

Kriegesmann, Benedikt, Raimund Rolfes, Christian Hühne, Jan Teßmer, and Johann Arbocz (2010). "Probabilistic Design of Axially Compressed Composite Cylinders With Geometric and Loading Imperfections". In: *International Journal of Structural Stability and Dynamics* 10.04, pp. 623–644. ISSN: 0219-4554. DOI: 10.1142/S0219455410003658. URL: http://www.worldscientific.com/doi/abs/10.1142/S0219455410003658.

Kriegesmann, Benedikt, Raimund Rolfes, Eelco L. Jansen, I. Elishakoff, C. Hühne, and Alexander Kling (2012). "Design optimization of composite cylindrical shells under uncertainty". In: *Computers, Materials and Continua* 32.3, pp. 177–200. ISSN: 15462218. URL: http://www.scopus.com/inward/record.url?eid=2-s2.0-84874823844&partnerID=tZOtx3y1.

Lam, By W F and C T Morley (1992). "Arc-Length Method for Passing Limit Points in Structural Calculation". In: *Journal of Structural Engineering* 118.1, pp. 169–185. ISSN: 0733-9445. DOI: 10.1061/(ASCE)0733-9445(1992)118:1(169).

Li, Chun-Ching and Armen Der Kiureghian (1993). "Optimal discretization of random fields". In: *Journal of engineering mechanics* 119.6, pp. 1136–1154. DOI: 10.1037/t21230-000.

Liu, Ling, Bo Ming Zhang, Dian Fu Wang, and Zhan Jun Wu (2006). "Effects of cure cycles on void content and mechanical properties of composite laminates". In: *Composite Structures* 73.3, pp. 303–309. ISSN: 02638223. DOI: 10.1016/j.compstruct.2005.02.001.

Minera, S., M. Patni, E. Carrera, M. Petrolo, P.M. Weaver, and A. Pirrera (2018). "Three-dimensional stress analysis for beam-like structures using Serendipity Lagrange shape functions". In: *International Journal of Solids and Structures* 141-142, pp. 279–296. ISSN: 00207683. DOI: 10.1016/j.ijsolstr.2018.02.030. URL: http://linkinghub.elsevier.com/retrieve/pii/S0020768318300866.

Pagani, A. and E. Carrera (2018). "Unified formulation of geometrically nonlinear refined beam theories". In: *Mechanics of Advanced Materials and Structures* 25.1, pp. 15–31. ISSN: 15376532. DOI: 10.1080/15376494.2016.1232458. URL: https://doi.org/10.1080/15376494.2016.1232458.

Papadopoulos, Vissarion and Manolis Papadrakakis (2004). "Finite-Element Analysis of Cylindrical Panels". In: *Managing* 130.August, pp. 867–876.

– (2005). "The effect of material and thickness variability on the buckling load of shells with random initial imperfections". In: *Computer Methods in Applied Mechanics and Engineering* 194.12-16, pp. 1405–1426. ISSN: 00457825. DOI: 10.1016/j.cma.2004.01.043.

Payette, G. S. and J. N. Reddy (2014). "A seven-parameter spectral/hp finite element formulation for isotropic, laminated composite and functionally graded shell structures". In: *Computer Methods in Applied Mechanics and Engineering* 278, pp. 664–704. ISSN: 00457825. DOI: 10.1016/j.cma.2014.06.021. URL: http://dx.doi.org/10.1016/j.cma.2014.06.021.

Reddy, Junuthula Narasimha (2014). *An Introduction to Nonlinear Finite Element Analysis: with applications to heat transfer, fluid mechanics, and solid mechanics*. OUP Oxford. ISBN: 2014935440.

Sasikumar, P., R. Suresh, P. K. Vijayaghosh, and Sayan Gupta (2015). "Experimental characterisation of random field models for CFRP composite panels". In: *Composite Structures* 120, pp. 451–471. ISSN: 02638223. DOI: 10.1016/j.compstruct.2014.10.023. URL: http://dx.doi.org/10.1016/j.compstruct.2014.10.023.

Schenk, C. A. and G. I. Schuëller (2007). "Buckling analysis of cylindrical shells with cutouts including random boundary and geometric imperfections". In: *Computer Methods in Applied Mechanics and Engineering* 196.35-36, pp. 3424–3434. ISSN: 00457825. DOI: 10.1016/j.cma.2007.03.014.

Spanos, P. D. and B. A. Zeldin (1998). "Monte Carlo Treatment of Random Fields: A Broad Perspective". In: *Applied Mechanics Reviews* 51.3, p. 219. ISSN: 0003-6900. DOI: 10.1115/1.3098999. URL: http://appliedmechanicsreviews.asmedigitalcollection.asme.org/article.aspx?articleid=1396252.

Sriramula, Srinivas and Marios K. Chryssanthopoulos (2013). "An experimental characterisation of spatial variability in GFRP composite panels". In: *Structural Safety* 42, pp. 1–11. ISSN: 01674730. DOI: 10.1016/j.strusafe.2013.01.002. URL: http://dx.doi.org/10.1016/j.strusafe.2013.01.002.

Tootkaboni, Mazdak, L. Graham-Brady, and B.W. Schafer (2009). "Geometrically non-linear behavior of structural systems with random material property: An asymptotic spectral stochastic approach". In: *Computer Methods in Applied Mechanics and Engineering* 198.37-40, pp. 3173–3185. ISSN: 00457825. DOI: 10.1016/j.cma.2009.05.014. URL: http://dx.doi.org/10.1016/j.cma.2009.05.014.

Varadhan, S. R. S. (1967). "On the behavior of the fundamental solution of the heat equation with variable coefficients". In: *Communications on Pure and Applied Mathematics* 20.2, pp. 431–455. ISSN: 00103640. DOI: 10.1002/cpa.3160200210. URL: http://doi.wiley.com/10.1002/cpa.3160200210.

Vryzidis, Isaak, George Stefanou, and Vissarion Papadopoulos (2013). "Stochastic stability analysis of steel tubes with random initial imperfections". In: *Finite Elements in Analysis and Design*

77, pp. 31–39. ISSN: 0168-874X. DOI: 10.1016/j.finel.2013.09.002. URL: http://dx.doi.org/10.1016/j.finel.2013.09.002.

Yurgartis, S.W. (1987). "Measurement of small angle fiber misalignments in continuous fiber composites". In: *Composites Science and Technology* 30.4, pp. 279–293. ISSN: 0266-3538. DOI: 10.1016/0266-3538(87)90016-9. URL: http://www.sciencedirect.com/science/article/pii/0266353887900169.